

Pressure effect on diffusion of carbon at the 85.91° ⟨100⟩ symmetric tilt grain boundary of α -ironMd Mijanur Rahman ^{1,*}, Fedwa El-Mellouhi ², Othmane Bouhali,³ Charlotte S. Becquart,⁴ and Normand Mousseau ^{1,†}¹*Département de Physique and Regroupement québécois sur les matériaux de pointe, Université de Montréal, C.P. 6128, Succursale Centre-Ville, Montréal, H3C 3J7 Québec, Canada*²*Qatar Environment and Energy Research Institute, Hamad Bin Khalifa University, P.O. Box 34110, Doha, Qatar*³*Texas A&M University at Qatar, Doha, Qatar*⁴*Université de Lille, CNRS, INRAE, Centrale Lille, UMR 8207, UMET, Unité Matériaux et Transformations, F-59000 Lille, France*

(Received 24 December 2020; accepted 1 April 2021; published 19 April 2021)

The diffusion mechanism of carbon in iron plays a vital role in carburization processes, steel fabrication, and metal dusting corrosion. In this paper, using the kinetic activation-relaxation technique (k-ART), an off-lattice kinetic Monte Carlo algorithm with on-the-fly catalog building that allows to obtain diffusion properties over large time scales taking full account of chemical and elastic effects coupled with an EAM potential, we investigate the effect of pressure on the diffusion properties of carbon in 85.91° ⟨100⟩ symmetric tilt grain boundaries (GB) of α -iron up to a pressure of 12 kbar at a single temperature of 600 K. We find that, while the effect of pressure can strongly modify the C stability and diffusivity in the GB in ways that depend closely on the local environment and the nature of the deformation, isotropic and uniaxial pressure can lead to opposite and nonmonotonous effects regarding segregation energy and activation barriers. These observations are relevant to understanding of the evolution of heterogeneous materials, where variations of local pressure can alter the carbon diffusion across the material.

DOI: [10.1103/PhysRevMaterials.5.043605](https://doi.org/10.1103/PhysRevMaterials.5.043605)**I. INTRODUCTION**

Metal dusting is a severe form of corrosion causing a catastrophic degradation of metals and alloys at high temperature in carbon-supersaturated gaseous environments. Engineering alloys such as low-alloy and stainless steels, as well as heat-resisting iron-, nickel-, and cobalt-base alloys catalyze gas processes that release carbon, leading to the formation of deposits at the surface of the alloy and, over time, to failure. In petrochemical plants and gas-to-liquid (GTL) production facilities, metal dusting has been observed in steel equipment. The so-called Fischer-Tropsch synthesis deposits carbon not only on the catalysts but also on the steel equipment, leading to dusting corrosion. The onset of metal dusting for iron-base alloys is initiated with saturation of the alloy matrix with carbon/carbides, usually in a localized manner, a process called carburization. In our earlier works we focused on carburization by characterizing reaction of iron with CO as well as the diffusion and segregation of carbon within the grain boundaries of the metal [1–9].

In this paper, we aim to turn our attention towards realistic scenarios that occur at various stages of dusting corrosion, drawing comparisons with experiments whenever possible, focusing more particularly on the effect of pressure on C diffusion in Fe, particularly at grain boundaries (GBs). The diffusion of carbon interstitial atoms around GBs in iron has long been an area of interest for researchers due to its impact

on various mechanical properties of steel such as corrosion resistance, and embrittlement, but also because it serves as a rich system for modeling and simulation [10,11]. Over the years, these mechanisms have been computationally studied at ambient pressure, i.e., the lattice and atomic positions are both relaxed to obtain the atomistic parameters at zero pressure [12–15]. While limited information is available regarding the effect of pressure on carbon diffusion in iron through GBs, internal or external pressures can build up in the grains due to local deformation. These may reach a magnitude of a few GPa [16–18], inducing problems such as structural instability, stress corrosion cracking, distortion, etc., [19–21]. It is thus necessary to have a clear description of the effects of pressure on defect diffusion in order to understand the behavior of heterogeneous materials such as carburized steels at the atomic scale.

Because of the microscopic nature of these processes, atomistic simulations are needed to provide an understanding of the details controlling these segregation and diffusion mechanisms that are difficult to obtain from experiments. While standard simulation tools, such as molecular dynamics, offer significant information on atomistic details of these diffusion mechanisms, they are often unable to reach the extended time scale over which many of these processes take place. Standard kinetic Monte Carlo (KMC) simulations provide a solution to reaching long-time dynamics, but, they are constrained to lattice-based displacements that fail to capture the full diversity of diffusion mechanisms as well as elastic deformations, especially around extended defects such as GB [22]. Over the years, numerous improvements have been proposed to standard KMC simulations, in order to overcome

*md.mijanur.rahman@umontreal.ca

†normand.mousseau@umontreal.ca

these limitations leading to an interest in the fundamental mechanisms associated with defect diffusion in materials. The recent development of on-the-fly off-lattice kinetic Monte Carlo methods such as the kinetic activation-relaxation technique (k-ART) [23–25] lifts those limitations and allows us to map these processes in details. k-ART is an off-lattice kinetic Monte Carlo method with on-the-fly catalog building capabilities, which enables to properly describe diffusion mechanism over experimentally-relevant time scales. It enables to reach simulated times many orders of magnitude longer than those reachable by MD simulation while incorporating exact elastic effects and identifying the atomistic details of diffusion mechanisms at every step.

In this study, using k-ART we investigate the effect of pressure on the diffusion mechanism C atom within a GB of α -iron. More precisely, we explore the energy landscape and kinetic pathways. Then, diffusion coefficients are calculated to quantify the effect of stress on diffusivity. The paper is organized as follows: the methodology, including a brief overview of k-ART, the model employed, and the computational details, is presented in Sec. II. Then, simulation results are presented and discussed in Secs. III and IV, respectively. Finally, the conclusion is given in Sec. V.

II. METHODOLOGY

A. Kinetic-activation relaxation technique (k-ART)

The kinetic activation-relaxation technique (k-ART) [23–25] is an off-lattice kinetic Monte Carlo (KMC) method with on-the-fly catalog building. k-ART is built around three tools: (i) NAUTY [26], which allows a topological characterization of the local environment surrounding each active atom; (ii) the activation-relaxation technique (ART nouveau or ARTn) [27–29], an open-ended saddle-search methods for exploring the local energy landscape; and (iii) a KMC algorithm [30] that evaluates the time between two steps and selects the event. The basic principles are briefly described below.

At the beginning of each KMC step, the local environment surrounding each atom is characterized by their local topology evaluated with NAUTY, a topological analysis library developed by McKay [26]. Graphs are generated by considering a sphere with a predefined radius (6 Å for the current system) around each atom in the system that contains around 75 atoms and drawing edges between all atoms within a cut-off distance of 2.7 Å of each other, a value that ensure that mostly only first-neighbor atoms are included. This connectivity graph is sent to NAUTY, which returns a unique identifier characteristic of its automorphic group.

If the topology is known, events associated with it are recovered from the catalog and placed in a KMC tree; otherwise, 100 ARTn searches are launched to identify the events associated with this topology. The ARTn search takes place in three steps: (i) first, the system is pushed in an arbitrary direction until the lowest eigenvalue of the Hessian matrix, determined using the Lanczos algorithm, becomes negative to confirm that the system is out of the harmonic well; (ii) then the system is pushed along the direction of the negative curvature and the force is minimized in the hyperplane perpendicular to this

direction after each push until the total force becomes lower than a predefined threshold value, indicating that a first-order saddle point is reached; and (iii) the system is then pushed over the saddle point and relaxed into a new minimum.

Once the catalog is fully updated and the tree is completed for the current atomistic configuration, generic events are ordered according to their rate, defined as

$$\Gamma_i = \nu_0 e^{-\frac{E_b}{k_B T}}, \quad (1)$$

where ν_0 is a fixed prefactor that is fixed at 10^{13} Hz and E_b is the activation energy for event i defined as the energy difference between the transition state and the initial minimum [31–33]. Once the event tree is completed, the lowest energy-barrier events that make up to 99.99% of the rate are fully reconstructed and reconverged into specific events to ensure that elastic and configurational effects are exactly taken into consideration. When this is done, specific rates and the overall KMC timestep are evaluated again, with the refined barriers, and an event is chosen according to standard KMC algorithm [30]. The elapsed time t is computed according to a Poisson distribution as

$$t = -\frac{\ln \mu}{\sum_i \Gamma_i}, \quad (2)$$

where μ is the random number uniformly distributed between 0 and 1.

To sum up, k-ART makes use of a unique topology classification coupled with an unbiased, open-ended search for saddle points, while considering short- and long-range interactions due to elastic effects. An extensive catalog of the events are created on-the-fly, which speeds up the simulation as the system evolves. In the past, k-ART has been used in various systems to describe diffusion of point defects in metals and semiconductors and more complex systems with grain boundaries and amorphous silicon [8,34,35].

B. Handling flickering states

KMC simulations can become inefficient in the presence of low-energy barriers that dominate the kinetics, as each step is then associated with a very small clock increase. In some cases, these events are flickers, a set of states, separated by low-energy barriers deep in a energy basin and that do not contribute to the evolution of the system. To avoid getting trapped by flickers, we use the basin-auto-constructing Mean Rate Method (bac-MRM) [25,36] to solve analytically the average residence time for the in-basin states. This method computes on-the-fly a statistically exact analytic solution of the connected flickering states and their escape rate as the energy landscape is explored, at the cost of specific trajectories. The bac-MRM is applied to all states connected by barriers and energy difference lower than a predefined threshold (0.5 eV is used in this study).

C. Interatomic potential

In order to access relevant length and time scales, we employ an empirical force field to describe the system. The Fe-Fe interactions are handled by the Embedded Atom Method (EAM) interatomic potential developed by Ackland

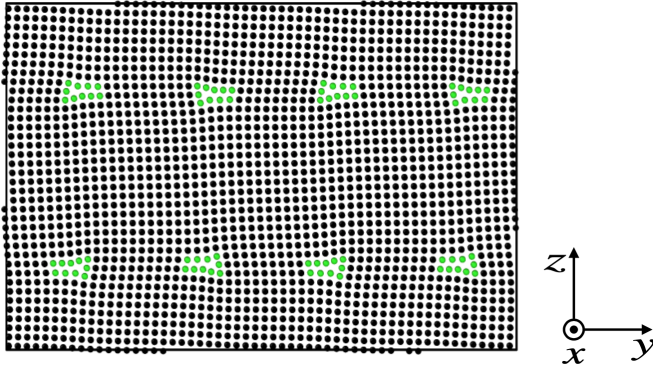


FIG. 1. Atomic arrangement representation of the 85.91° $\langle 100 \rangle$ tilt GB in bcc Fe after 1 ns of initial relaxation using molecular dynamics (MD) at zero pressure and temperature 600 K prior to starting k-ART simulations. Black circles represent Fe atoms having a crystalline bcc local environment, while green circles represent atoms having a non-bcc environment surrounding the GB. The GB rotation axes $\langle 100 \rangle$ are parallel to the x axis out of planes, while GB planes are perpendicular to the z axis.

and Mendeleev [37] while the Fe-C interaction part was developed by Becquart and collaborators [38,39]. The combined potential provides a good agreement with DFT calculations in bulk system [7]. This potential has been used with success to model the effect of the stress field of an edge dislocation on carbon diffusion, the formation of carbon Cottrell atmospheres in bcc iron as well as the elastic constants of the martensite [40–42]. For all calculations, k-ART uses the LAMMPS library to compute the forces and energies [43,44].

D. Simulation details

Two simulation boxes are used in this paper. The first one consists in a perfect cubic bcc bulk crystal containing 2000 iron atoms. The second box is a bcc system containing 25 537 atoms featuring a 85.91° $\langle 100 \rangle$ tilt GB with dimensions of $34.332 \text{ \AA} \times 113.090 \text{ \AA} \times 76.595 \text{ \AA}$. To allow periodic boundary conditions in all directions, the box contains two GBs separated by a distance equal to half the box size in the z direction. The 85.91° $\langle 100 \rangle$ structure is a general GB with GB energy per unit area, $E_{\text{GB}} = 37.118 \text{ meV/\AA}^2$. This GB Fe system was chosen because of its structural stability, and the presence of a number of sites where C can be trapped, allowing us to focus on the effect of deformation impurity diffusion. An atomistic representation of the GB is shown in Fig. 1. To determine the appropriate simulation volume, the system boxes, with a C interstitial, are equilibrated at the targeted pressure at 600 K temperature by performing NPT ensemble with LAMMPS. The volume is then fixed for k-ART simulations.

For each simulation, the ground state (GS) energy is defined as the lowest energy minimum identified during the run, E_{GS} . The activation energy for an event is defined as the energy difference between the initial minimum E_{min} and the saddle E_{sad} (i.e., the barrier crossed between two adjacent minima) or

$$E_b = E_{\text{sad}} - E_{\text{min}}. \quad (3)$$

The effective barrier is defined as the total barrier crossed when jumping from one GS to another GS.

The square displacement (SD) is computed as usual,

$$SD = \sum_i^N (r_i(t_n) - r_i(0))^2, \quad (4)$$

where N is the number of particles and $r_i(t_n)$, the position of atom i at KMC step n .

To ensure sufficient statistics, the diffusion coefficient of carbon interstitial atom calculated using the embedded discrete time Markov chain (EDTMC) described as follows:

- (1) choose an initial state i ;
- (2) generate a uniform random number $u \in (0, 1]$;
- (3) select the next event j probabilistically such that $\sum_k^{j-1} p_{ik} < u \leq \sum_k^j p_{ik}$, where, p_{ik} is the probability to jump from state i to state k ;
- (4) update the total selection number of state j by adding 1;
- (5) update the current state $j \rightarrow i$; and
- (6) return to step 2.

EDTMC uses the transition matrix obtained from k-ART and that includes all the structurally different sites in which C visited and the mapped connectivity between the sites and their associated relative transition rates. For all coefficient diffusion results presented here, we run 600 million EDMC steps to obtain the relative frequency distribution $\bar{\Pi}$,

$$\bar{\Pi} = [\pi_1 \quad \pi_2 \quad \dots \quad \pi_m] \quad (5)$$

where π_i represents the proportion of times that site i is selected and m is the total number of structurally different sites in the system, for instance, in the case of perfect bulk crystal there are structurally three different sites directed along x, y, or z (see Fig. S1 in Supplemental Material [45]).

After obtaining the relative frequency distribution, we then calculate the average time $\langle t \rangle$ and average square displacement $\langle SD \rangle$:

$$\langle t \rangle = \sum_{i=1}^m \pi_i \tau_i, \quad (6)$$

$$\langle SD_l \rangle = \sum_{i=1}^m \sum_{j=1}^m \pi_i p_{ij} (\lambda_{ij}^l)^2, \quad (7)$$

with $l = x, y, z$, and

$$\langle SD \rangle = \langle SD_x \rangle + \langle SD_y \rangle + \langle SD_z \rangle, \quad (8)$$

where τ_i is the mean residence time at site i , p_{ij} is the transition probability from site i to site j and $p_{ij} = 0; \forall i = j$. λ_{ij}^l correspond to the $l = x, y, z$ components of the displacement vectors for the jump from site i to site j , respectively.

The total diffusion coefficient is calculated as

$$D = \frac{\langle SD \rangle}{2n_d \langle t \rangle}, \quad (9)$$

where n_d is the dimensionality of the motion [(1)–(3)].

III. RESULTS

A. Carbon in bulk iron

First we analyze the effect of pressure on the evolution of a single C atom in crystalline α -Fe. In the ground state, the C atom occupies the octahedral interstitial position, located in the middle of one of the three edges of the cubic unit cell (see Fig. S1 in the Supplemental Material [45]); it migrates, following its dominant pathway, by going through an adjacent tetrahedral site that represents the transition state. With respect to the orientation of the two closest Fe atoms, three octahedral variants directed along x, y, or z can be identified. These are energetically equivalent in the perfect BCC lattice, but split into two nonequivalent types under uniaxial deformation: a distortion along x axis divides the octahedral sites into O_x and $O_y \equiv O_z$ (see Fig. S2 in the Supplemental Material [45]).

Recently, Tchitchekova *et al.* [41], using a method called Linear Combination of Stress States (LinCoSS), evaluated the effects of simple-heterogeneous uniaxial and shear stresses on the migration energies of C in bulk Fe. In this section, we reproduce this result for a C in bulk Fe with a thermally-adjusted density corresponding to 600 K, but also consider isotropic deformations and extract the diffusion coefficient for each of these deformations.

The variation of the crystalline lattice parameter and of the system's enthalpy as a function of isotropic pressure are shown in Fig. 2(a), while the evolution of the activation energy for an interstitial C atom as it jumps from one octahedral site to a nearest octahedral site and the diffusivity of C as a function of pressure are plotted in Fig. 2(b). Both the diffusion activation energy and the total enthalpy show a positive correlation with isotropic pressure over the full range considered here. The variation of activation energies E_b and that of the total enthalpy follows a quadratic form with the values for the constant, linear, and quadratic parameters listed in Table S1 in the Supplemental Material [45].

The effects of uniaxial pressure (along x axis) and biaxial pressure (along y and z axes) are shown in Figs. 3 and 4. Figures 3(a) and 3(b) present the activation energy of for an interstitial C atom as it jumps from one octahedral site to a nearest octahedral site as a function of uniaxial pressure and biaxial pressure, respectively. Activation energies from O_x to $O_y(\equiv O_z)$, from $O_y(\equiv O_z)$ to O_x and from O_y to O_z follow a quadratic curve (values of the linear parameters and quadratic parameter listed in Table S1 in the Supplemental Material [45]). Figures 4(a) and 4(b) show the C diffusion coefficient at temperature 600 K at each directions as a function of uniaxial and biaxial pressure, respectively. Calculated activation volume V^{act} , activation barrier E^{act} , and diffusion prefactor D_0 are listed in Table S2 in the Supplemental Material [45]. We find that $D_y(\equiv D_z) < D_x$ under uniaxial compression and $D_y(\equiv D_z) > D_x$ under uniaxial expansion with the the ratio D_x/D_y approximately inversed when the pressure changes sign [see Fig. 4(c)].

Under uniaxial compression along the x axis, the O_y and O_z octahedral sites are more energetically stable sites than the O_x octahedral sites by as much as 0.132 eV at 24 kbar (see Fig. S2 in the Supplemental Material [45]), with barriers going from O_y (O_z) to O_x lower by as much as 0.051 eV

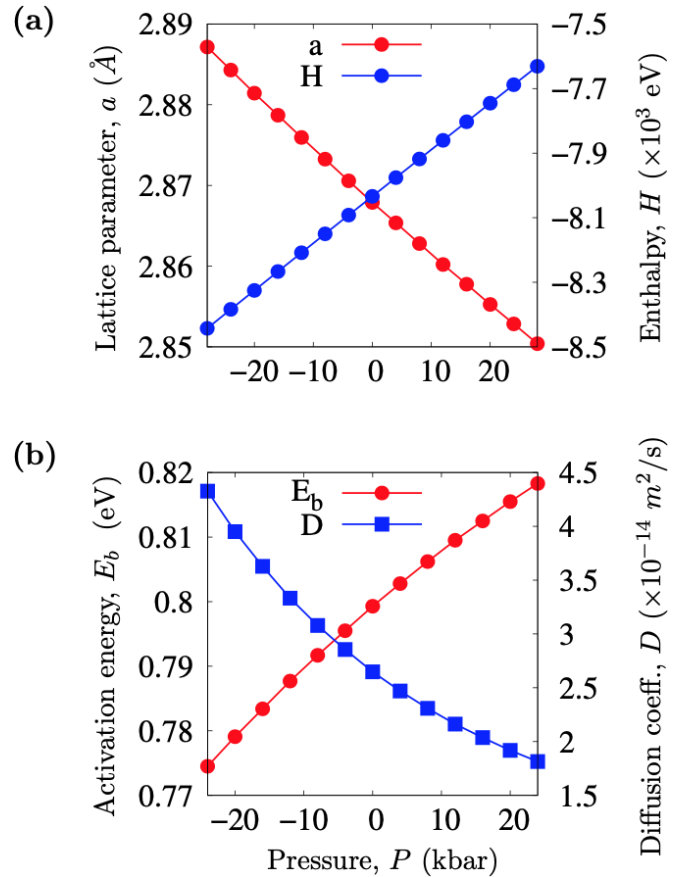


FIG. 2. (a) Enthalpy variation for a single carbon in 2000-atom Fe bulk crystal (blue circles) and crystal lattice parameter (red circles) as a function of isotropic pressure. (b) Variation of the activation energies (red circles) and diffusion coefficients (blue squares) as a function of pressure for a single carbon atom in the same system. Diffusion coefficient is calculated with EDTMC and Eq. (9).

as compared with O_y (O_z) to O_x . Consequently, the lowest energy-diffusion pathway for C interstitial goes from O_y to O_z to O_y , channeling the C atom along the contracted axis. Therefore, the axial compression promotes axial diffusion. On the contrary, axial expansion promotes transverse in-plane diffusion along the chain (O_y or O_z) \rightarrow O_x \rightarrow (O_y or O_z) \rightarrow O_x (detailed C diffusion trajectories obtained with k-ART under uniaxial deformation are shown in Fig. S3 in the Supplemental Material [45]).

Since the contraction along x direction is equivalent to expansion along y and z direction, biaxial deformation just reverses the tendency: biaxial compression promotes C diffusion along the y-z in-plane while the biaxial expansion promotes x-channeling diffusion.

B. Carbon in the grain boundary

To relieve the pressure created on the crystalline network, interstitial impurities such as C tend to segregate towards defects, such as grain boundaries (GB), where there is more free volume than on the crystalline bulk side. This segregation propensity depends, of course, on specific binding sites at the GB and is characterized by the segregation energy defined as

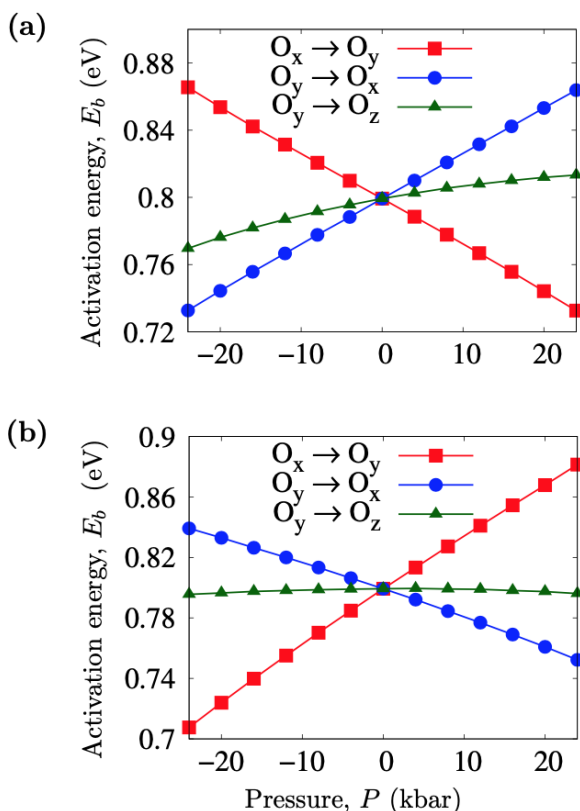


FIG. 3. Variation of the activation energy for C diffusion in the bulk iron at 600 K as a function of (a) uniaxial and (b) under biaxial stress. The red square, blue circle, and green triangle represent the carbon diffusion between octahedral variants $O_x \rightarrow O_y$, $O_y \rightarrow O_x$ and $O_y \rightarrow O_z$, respectively.

the difference between the energy of the system with C in a particular site and that in the octahedral site in the crystal side. A negative value of segregation energy means that the grain boundary site is energetically more favorable than the bulk site and signals a general flux from the bulk to these sites at the GB.

As demonstrated in our previous work [8], the disorder associated with GB generates a variety of atomic environments, facilitating the formation of sites more energetically favorable to the presence of carbon than interstitial crystalline sites. Depending on the specific nature of the interface between the grains, these favorable sites could be connected to accelerate or to slow down carbon diffusion as compared to the bulk. In the specific case studied here, we add that, segregation energies as well as related C migration barriers are reported in this paper differ from the value found in our previous work [8] as they are identified differently: sites identified in the previous work were generated kinetically through C migration from the bulk to the GB [8] while a direct extensive search for C sites, with simulations launched from different GB sites, was performed for the current work to identify the thermodynamically preferential sites. While this approach leads to different diffusion pathways, it does not affect the validity of our previous analysis.

k-ART search for C diffusion pathways at the 85.91° GB finds six different connected sites, with a segregation energy

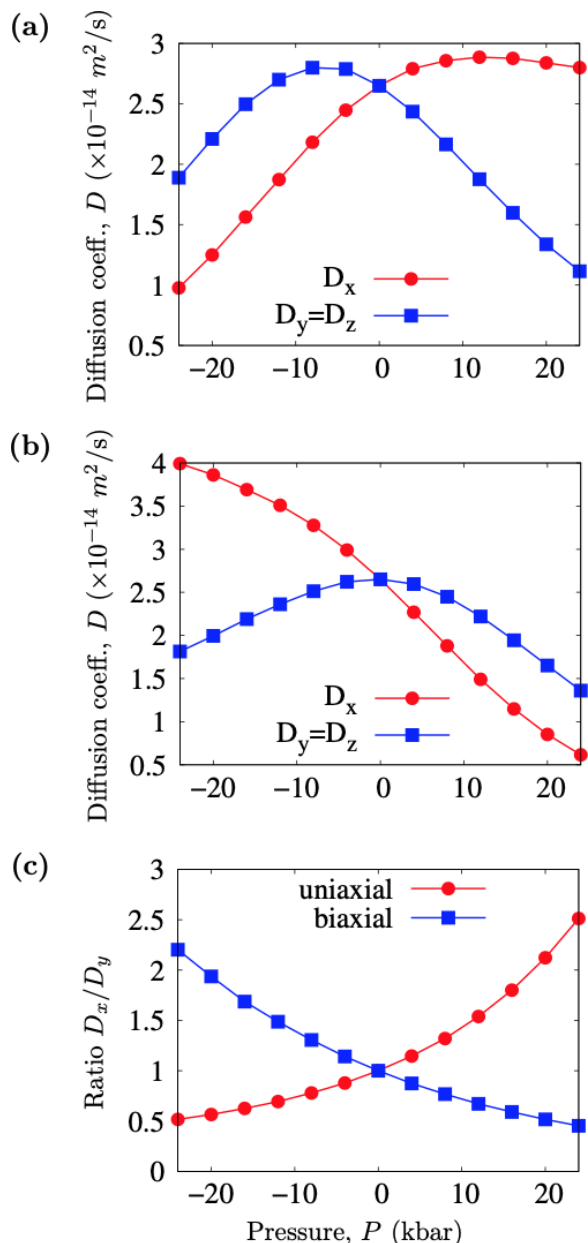


FIG. 4. C diffusion coefficient in the bulk crystal at 600 K as a function of (a) uniaxial stress, (b) under biaxial and (c) ratio D_x/D_y . All the values are calculated using EDTMC and Eq. (9).

ranging from -0.745 eV to 0.180 eV at zero pressure. Figure 5 represents the four most energetically favorable sites for carbon segregation (S_0 to S_3), along with their segregation energy, measured with respect to the bulk ground state for C at zero pressure, and activation energies for diffusion between these sites. Further details, including shortest Fe-C bond length, coordination number, and segregated energies under various static deformations, are listed in Table I. The coordination number is defined as the number of neighboring Fe atoms within a cut-off distance of 2.47 \AA from the C atom. As previously found for this specific grain boundary [8], even the highest energy states along the dominant diffusion pathways at the GB are lower than the bulk ground state, which indicates a strong segregation tendency of C atoms to the GB. At the

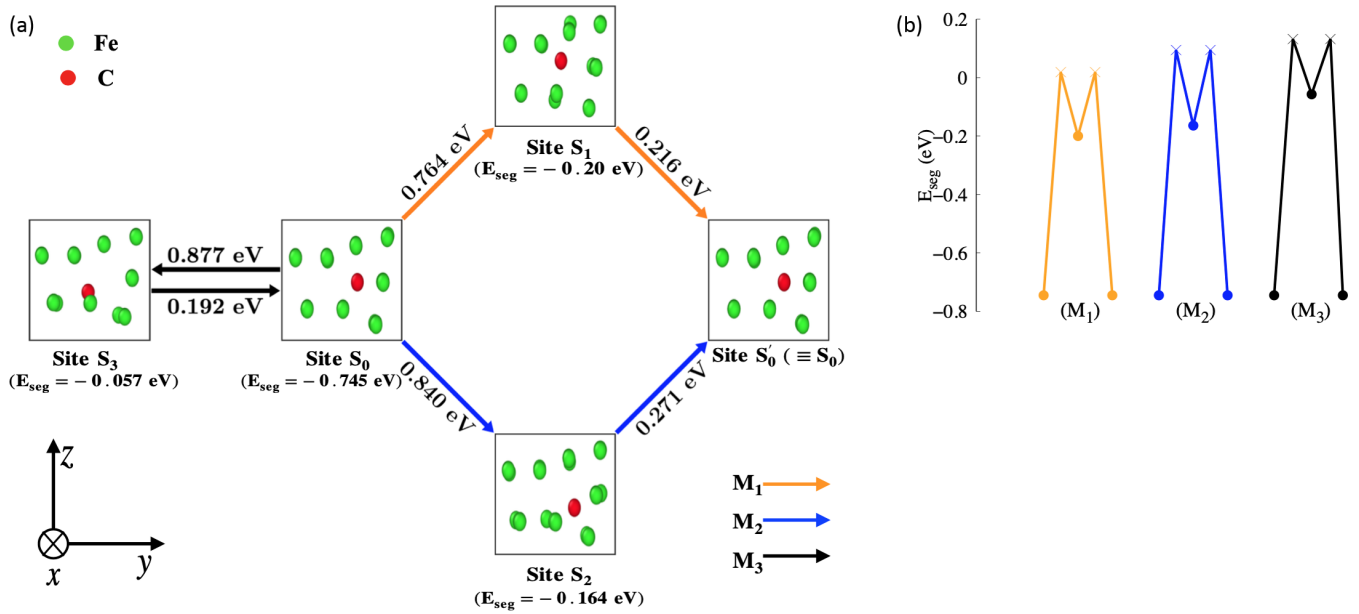


FIG. 5. (a) Atomistic representation of three most frequent diffusion mechanisms of carbon atom at the dislocation core in GB at zero pressure. The orange, blue, and black lines indicate mechanisms M_1 , M_2 , and M_3 , respectively. M_1 and M_2 can move the C atom into a new final configuration (S'_0) (equivalent to the initial configuration (S_0) with the impurity jumping by one lattice spacing along the x direction); M_3 brings the C atom back to its initial configuration (S_0). It does not contribute to the net diffusion. (b) The minimum energy pathway for the different mechanisms is shown, where the circles and crosses represent minimum and saddle points, respectively. E_{seg} is the relative energy with respect to the bulk ground state for C.

GB, the lowest energy state at the GB is labeled S_0 (situated at the center of the dislocation core of the GB), with a segregation energy of -0.745 eV. Among the four lowest-energy states (S_0 to S_3), S_0 shows the highest coordination number, with the longest Fe-C nearest-neighbor distance associated with a low-stress environment as compared with the bulk site (Table I).

Figures 6(a)–6(c) represent the variation of the segregation energies for these four lowest-energy sites as a function of isotropic pressure as well as uniaxial (along x axis: direction of GB) and biaxial (along y and z axes: plane perpendicular to the GB direction) deformations. Within a range of -12 to 12 kbar, the segregation energy of the C at each binding site tends to evolve linearly, although the slope varies with specific sites. The displayed relative energy shows that all C binding sites at the GB become more stable as compared to the interstitial octahedral sites of the crystal side under isotropic compression. As the pressure is increased from 0 to

12 kbar, the segregation energy of C at the most stable site (S_0) increases in stability by 0.077 eV, whereas the segregation energy of C at sites S_1 , S_2 , and S_3 increases in stability by 0.02 , 0.034 , and 0.032 eV, respectively. A similar behavior is observed under biaxial pressure. However, sites S_1 , S_2 , and S_3 are even more favored, as compared to the case of isotropic pressure, with increasing the pressure (values listed in Table I). Under biaxial compression, the two Fe nearest-neighbors are displaced along the x direction, leaving more space for the C atom. Interestingly, the segregation energy of sites S_0 remains unaffected by uniaxial deformation, since the radius of the dislocation core is unaffected by the deformation. Hence, the increment (or decrement) in the total energy of the C at site S_0 and the octahedral site in the crystal side are almost same under uniaxial pressure. In contrast to isotropic and biaxial pressure, the sites S_1 , S_2 , and S_3 are destabilized under uniaxial compression.

TABLE I. Values of the coordination number, shortest Fe-C bond length, and segregation energies of four most stable sites at the GB region at different pressures.

Site	Coordination No.	Isotropic pressure																	
		0 kbar		12 kbar				-12 kbar				Pressure applied along x axis				Pressure applied y and z axes			
		$d_{\text{Fe-C}}^{\text{min}}$ (Å)	E_{seg} (eV)																
S_0	8	2.029	-0.745	2.028	-0.822	2.031	-0.660	2.023	-0.740	2.033	-0.735	2.032	-0.814	2.010	-0.673				
S_1	5	1.764	-0.20	1.763	-0.220	1.765	-0.174	1.768	-0.190	1.763	-0.206	1.763	-0.230	1.766	-0.164				
S_2	5	1.775	-0.164	1.774	-0.198	1.775	-0.123	1.776	-0.120	1.773	-0.178	1.772	-0.214	1.775	-0.080				
S_3	5	1.819	-0.057	1.818	-0.089	1.820	-0.017	1.813	0.013	1.823	-0.091	1.823	-0.126	1.812	0.028				

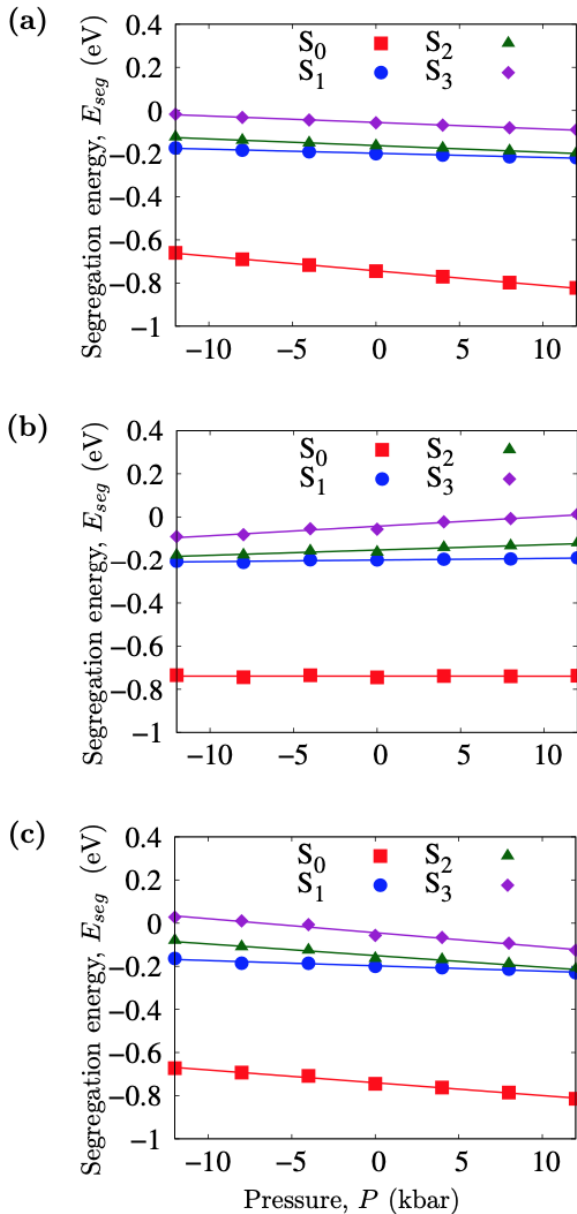


FIG. 6. Segregation energy as a function of pressure for a C atom at the 85.91° GB: (a) under isotropic pressure, (b) pressure along the x direction, and (c) pressure applied along the plane perpendicular to the GB plane. Red square, blue circle, green triangle, and violet diamond correspond to carbon at the site S_0 , S_1 , S_2 , and S_3 , respectively.

After characterizing the change in stability of the dominant segregation sites under pressure, we now turn to the effect of pressure on the C activation energies and diffusion pathways at the 85.91° GB. C diffusion at the GB is complex as compared with that of the crystalline bulk. As demonstrated in previous work [8], at zero pressure, C diffusion occurs through several pathways that move through the most favorable GB sites (the energy details of all available events and the histogram of the activation energy barrier for selected events at 600 K for a single C at GB during the 12 000 KMC steps are shown, respectively, in Fig. S3 and Fig. S4 in the Supplemental Material [45]). Figure 5 provides an atomistic representation of the three most frequent C diffusion local

pathways at the GB that we label as M_1 , M_2 , and M_3 . Each pathway is a two steps process: C diffuses from the ground state (site S_0) to a metastable state (S_1 , S_2 , or S_3), then from this metastable state to a new GS (site $S'_0 = S_0$). While, after these two jumps, M_1 and M_2 can reach a new lower-energy state, dubbed S'_0 , M_3 systematically brings the C back to its initial position when following the lowest-energy pathways and, as such, does not contribute to diffusion. M_1 exhibits the lowest maximal energy barrier, which makes mechanism M_1 the most probable. At zero pressure, the first step of mechanism M_1 requires crossing an energy barrier of 0.764 eV to reach S_1 . From there the C then crosses a 0.216 eV barrier to complete the migration into a new S_0 site. The second (M_2) and third (M_3) low-energy diffusion mechanism are associated with effective barriers of 0.840 and 0.877 eV, respectively, compared to 0.810 eV in the bulk.

The variation of the effective energy barriers for the three dominant pathways at the GB along with their selection's frequency as a function of pressure is shown in Fig. 7. Within a pressure range of -12 to 12 kbar, the effective barrier associated with M_1 , M_2 , and M_3 varies linearly with pressure, but at different rate. In the case of isotropic deformation, as the pressure is increased from 0 to 12 kbar, the effective barriers associated with the dominant diffusion mechanism (M_1) increase by 0.111 eV, whereas the effective barriers for mechanism M_2 and M_3 increase by 0.055 and 0.045 eV, respectively. Since, the energy gap between the pathway's effective barriers narrows as pressure is increased, the less probable mechanisms (such as M_3) become more frequent under isotropic compression at temperature 600 K. In the case uniaxial deformation, on the contrary, the energy gap between the pathway's effective barriers widen and mechanism M_1 become even more dominant under compression. As the pressure is increased from 0 to 12 kbar the effective barriers associated with the diffusion mechanism M_1 , M_2 , and M_3 increase by 0.014, 0.028, and 0.053 eV, respectively. By contrast to the isotropic and uniaxial pressure, effective barriers associated with the diffusion mechanism M_3 decreases under biaxial compression. As the pressure is increased from 0 to 12 kbar, the effective barriers associated with the diffusion mechanism (M_3) decrease by 0.003 eV, whereas the effective barriers for mechanism M_1 and M_2 increase by 0.078 and 0.017 eV, respectively.

C diffusion at 85.91° $\langle 100 \rangle$ tilt GB is largely restricted to the interface and diffusion take place mostly along the x axis (diffusion trajectories obtained with k-ART at different pressure are shown in Fig. S6 in the Supplemental Material [45]).

To extract a converged diffusion coefficient, we turn, as discussed in the method section, to a Markov chain solution on a transition probability matrix (the size of which ranges from 5×5 – 7×7 depending of the nature of the deformation) that incorporates the full set of events identified with k-ART, irrespective of their energy barrier. Figure 8(a) shows the variation of C diffusion coefficient at the GB under isotropic pressure along the x, y, and z axes at temperature 600 K. Figure 8(b) represents the Arrhenius plot for C diffusivity in GB. The calculated activation volume V^{act} , activation barrier E^{act} , and diffusion prefactor D_0 are listed in Table S2 in the Supplemental Material [45]. We find that it decreases (increases) linearly under lattice compression (expansion), but

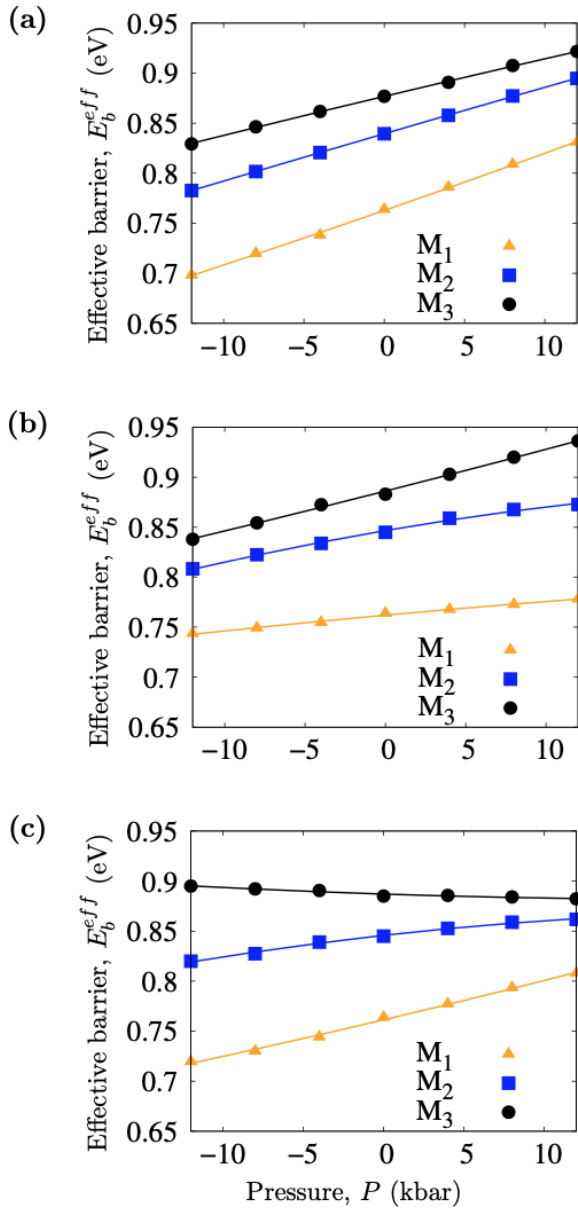


FIG. 7. Variation of the effective barrier of the diffusion mechanism M_1 , M_2 , and M_3 as a function of pressure: (a) under isotropic pressure, (b) pressure along the x direction, and (c) pressure applied along the plane perpendicular to the GB plane.

at different rates. Under lattice compression, as the pressure is increased from 0 to 12 kbar, the diffusion coefficient of C at the GB is decreased by $1.39 \times 10^{-13} \text{ m}^2\text{s}^{-1}$ (net effective barrier increase: 0.068 eV), $5.30 \times 10^{-14} \text{ m}^2\text{s}^{-1}$ (net effective barrier increase: 0.01 eV), and $1.03 \times 10^{-13} \text{ m}^2\text{s}^{-1}$ (net effective barrier increase: 0.046 eV) for the isotropic, uniaxial, and biaxial pressure, respectively. On the other hand, under lattice expansion as the negative value of pressure is increased from 0 to 12 kbar, the diffusion coefficient of C at the GB is increased by $4.95 \times 10^{-13} \text{ m}^2\text{s}^{-1}$ (net effective barrier decrease: 0.067 eV), $1.09 \times 10^{-13} \text{ m}^2\text{s}^{-1}$ (net effective barrier decrease: 0.020 eV), and $2.15 \times 10^{-13} \text{ m}^2\text{s}^{-1}$ (net effective barrier decrease: 0.047 eV) for the isotropic, uniaxial, and biaxial pressure, respectively.

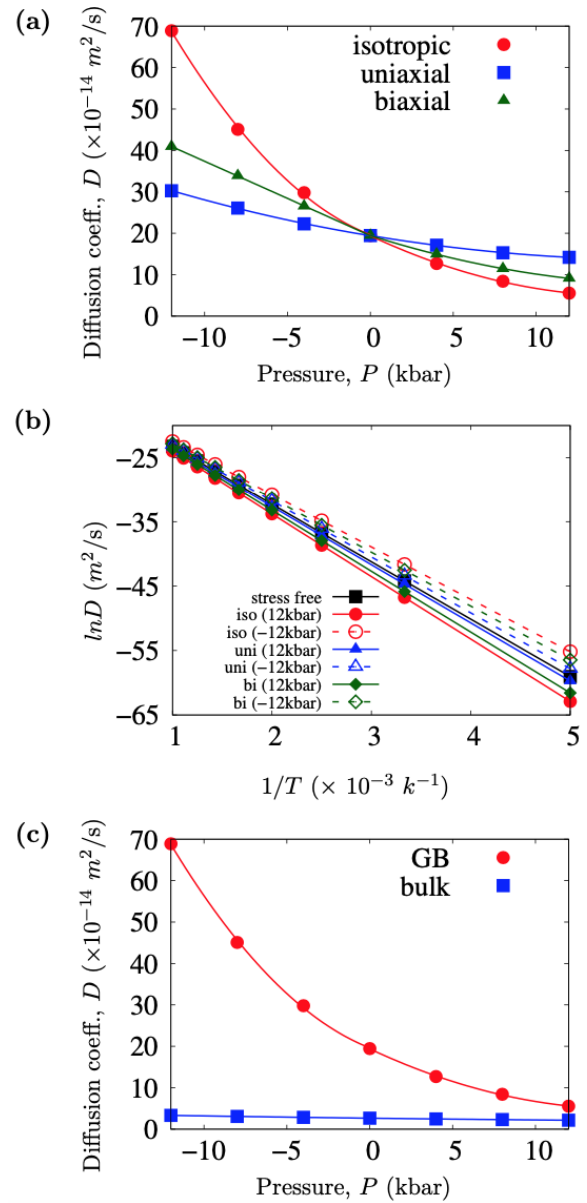


FIG. 8. (a) Variation of the C diffusion coefficient at the GB as a function of pressure: red circle, blue square, and green triangle represent the applied pressure isotropic, along x axis, and along y and z axes, respectively. (b) Arrhenius plot of the diffusivity of C in GB: red, blue, and green line represent for the applied pressure isotropic, along x axis, and along y and z axes, respectively. Black line refers to stress-free conditions. (c) Variation of the diffusion coefficient of C as a function of isotropic pressure: red circle and blue square represent C at the GB and crystalline bulk, respectively. Results presented here are calculated using Eq. (9).

Figure 8(c) compares the results for a similar set of calculations for the C diffusion coefficient at the GB and in the crystalline bulk under isotropic pressure at 600 K. We find that the applied pressure strongly affects C diffusivity at the GB as compared to bulk. At zero pressure, C diffusion at the GB is faster than in the crystalline bulk: the diffusion coefficient of C at GB is $1.94 \times 10^{-13} \text{ m}^2\text{s}^{-1}$ (corresponds to an effective barrier 0.772 eV), which is order of magnitude

higher as compared with $2.65 \times 10^{-14} \text{ m}^2\text{s}^{-1}$ (corresponds to a barrier of 0.810 eV) in the crystalline bulk. The diffusivity of C at GB decreases rapidly as compared in bulk when isotropic pressure increases: as the pressure is increased from 0 to 12 kbar the diffusion coefficient of C at GB decreased by $1.39 \times 10^{-14} \text{ m}^2\text{s}^{-1}$ (net effective barrier increase: 0.068 eV) compared with $4.9 \times 10^{-15} \text{ m}^2\text{s}^{-1}$ (net barrier increase: 0.01 eV) in the crystalline bulk.

IV. DISCUSSION

To understand the impact of pressure on impurity diffusion at grain boundaries, we first establish a reference case by considering impurity diffusion in the bulk crystal under isotropic, uniaxial, and biaxial deformations. In agreement with simulations done on a system equilibrated at $T = 0 \text{ K}$ [41], we find that the activation energy barrier increases under isotropic pressure. We show that this leads to a nonlinear reduction in the diffusion coefficient, as should be expected. A similar observation was made in experiments of vacancy-mediated In diffusion in Cu [46,47], which suggest that this slowing down, in a dense metallic system is associated with the reduced space available along the diffusion pathway between two stable states.

Uniaxial and biaxial compressions, by breaking symmetry, introduce divergence in activation energy as a function of jump directions for the interstitial C, with some barriers decreasing while others increase under increasing pressure, leading to a nonmonotonous effect of pressure on the diffusion coefficient. This nonmonotonous effect can be explained by the fact that, in addition to making the lattice stiffer, increasing pressure raises the formation energy for an interstitial. Along some diffusion directions, the enthalpy at the stable site increases faster than that at the transition state, leading to an effective reduction in the diffusion barrier.

These effects are made more complex at the grain boundary due to an increased richness in the energy landscape. This explains why results on various GBs differ. For example, Lojkowski *et al.* looking at In diffusion at a Cu grain boundaries, find that diffusivity increases with pressure [46,47] while it decreases by an order of magnitude for Zn diffusing along tilt GBs in Al as the pressure is raised to 12 kbar [48].

Recently, Karki *et al.* [49] performed first-principles simulations, based on density functional theory, on the $\{310\}/[001]$ tilt GB in MgO. They showed that native defects and impurities (Ca, Al, and proton) favorably segregate to the GB with the segregation considerably increasing with pressure. The authors also remarked that the impurity diffusion is faster at the GB as compared to the bulk as the pressure is increased as they showed that migration energies for host ions and impurities at the grain boundary are smaller than the bulk values, more so at higher pressures with their values being as low as 1.5 eV at 100 GPa compared to the bulk values of 4 eV.

Using k-ART, we obtain a more complete picture of the energy landscape of our system, C at the $85.91^\circ \langle 100 \rangle$ tilt GB. We find that, while segregation energy tends to become more favorable to the GB with respect to the bulk for a C interstitial with increasing isotropic pressure, the gain depends on specific sites, with some barely changing moving over a 24-kbar pressure change. Moreover, we observe that the orientation of

pressure with respect to the GB changes the result: applying a pressure normal to the GB reduces the available free volume at the GB and, therefore, reduces the segregation energy, while a pressure parallel to the GB plane increases the formation enthalpy in the bulk while preserving a larger free volume, and increasing the energy gain of moving to the GB.

Pressure will also affect the various transition states differently as is shown in our detailed analysis of its effect for the three dominant transition states at the GB. While all three barriers increase linearly under increasing isotropic and normal pressure, albeit with a different slope, this is not the case for pressure applied parallel to the GB plane, which could, at high enough pressure, lead to a change in the dominant diffusion mechanisms and the overall diffusion. This suggests that inhomogeneities in materials that can create large local pressure fluctuations will increase the complexity of impurity diffusion and could favor mechanisms that are missed in analyses that do not explore the full landscape but could affect the overall properties of the material. k-ART provides a complete picture about evolution of C within a representative grain boundary under the influence of pressure, thus mimicking realistic working conditions and providing unique long-time description of the evolution of the system. The resulting full-energy landscape on the impact of pressure on the C diffusion in iron once combined with surface phenomena can be regarded as one of the key parameters to determine the threshold and peak carburization rates of Fe surfaces.

V. CONCLUSIONS

Using the kinetic activation-relaxation technique, an off-lattice kinetic Monte Carlo method with on-the-fly catalog generation, we study pressure effect on the C diffusion in GB of α -iron providing detailed information regarding mechanisms and pathways that is difficult to obtain through standard simulation methods. Our results show a richness in the diffusion mechanisms as well as a complex balance between elastic and chemical effects.

In particular, the effect of pressure can strongly modify the C stability and diffusivity in GB. These effects vary between isotropic and uniaxial pressure, with segregation energies of various metastable sites moving in opposite directions, in some cases. This can have a major impact on the evolution of heterogeneous materials, with variations of local pressure that would strongly alter diffusion across the material.

More work is required to better characterize this behavior and extract general rules. Clearly, additional simulations are needed to assess how multiple C interstitial atoms or other defects such as vacancies and substitutional atoms diffuse at GBs under pressure; simulations are underway. The detailed analysis of the energy landscape provided by k-ART, however, shows that it is necessary to take specific mechanisms into account, with the possibility of developing precise control on the evolution of impurities in complex materials under local and global deformations.

Various ART nouveau implementations are available at our website [50] for free download. The most recent packages for k-ART and ART nouveau are available freely from the authors upon request.

ACKNOWLEDGMENTS

This work has been supported by the Qatar National Research Fund (QNRF) through the National Priorities Research Program under Project No. NPRP10-0105-170118 and by a

Discovery Grant from the Natural Sciences and Engineering Research Council of Canada (NSERC). We are grateful to Calcul Qubec/Compute Canada (CQ/CC) for generous allocations of computer resources.

- [1] I. H. Sahputra, A. Chakrabarty, O. Restrepo, O. Bouhali, N. Mousseau, C. S. Becquart, and F. El-Mellouhi, Carbon adsorption on and diffusion through the Fe (110) surface and in bulk: Developing a new strategy for the use of empirical potentials in complex material set-ups, *Phys. Status Solidi B* **254**, 1600408 (2017).
- [2] A. Chakrabarty, O. Bouhali, N. Mousseau, C. S. Becquart, and F. El-Mellouhi, Insights on finite size effects in *ab initio* study of co adsorption and dissociation on Fe 110 surface, *J. Appl. Phys.* **120**, 055301 (2016).
- [3] S. O. Akande, E. T. Bentia, O. Bouhali, and F. El-Mellouhi, Searching for the rate determining step of the H₂S reaction on Fe (110) surface, *App. Surf. Sci.* **532**, 147470 (2020).
- [4] A. Chakrabarty, E. Bentría, S. Omotayo, O. Bouhali, N. Mousseau, C. Becquart, and F. El-Mellouhi, Elucidating the role of extended surface defects at Fe surfaces on co adsorption and dissociation, *Appl. Surf. Sci.* **491**, 792 (2019).
- [5] E. Bentría, G. N'tsouaglo, C. Becquart, O. Bouhali, N. Mousseau, and F. El-Mellouhi, The role of emerging grain boundary at iron surface, temperature and hydrogen on metal dusting initiation, *Acta Mater.* **135**, 340 (2017).
- [6] A. Chakrabarty, O. Bouhali, N. Mousseau, C. Becquart, and F. El-Mellouhi, Influence of surface vacancy defects on the carburisation of Fe 110 surface by carbon monoxide, *J. Chem. Phys.* **145**, 044710 (2016).
- [7] O. A. Restrepo, N. Mousseau, F. El-Mellouhi, O. Bouhali, M. Trochet, and C. S. Becquart, Diffusion properties of Fe-C systems studied by using kinetic activation-relaxation technique, *Comput. Mater. Sci.* **112**, 96 (2016).
- [8] O. A. Restrepo, N. Mousseau, M. Trochet, F. El-Mellouhi, O. Bouhali, and C. S. Becquart, Carbon diffusion paths and segregation at high-angle tilt grain boundaries in α -Fe studied by using a kinetic activation-relation technique, *Phys. Rev. B* **97**, 054309 (2018).
- [9] O. Restrepo, C. Becquart, F. El-Mellouhi, O. Bouhali, and N. Mousseau, Diffusion mechanisms of C in 100, 110 and 111 Fe surfaces studied using kinetic activation-relaxation technique, *Acta Mater.* **136**, 303 (2017).
- [10] S. Suzuki, M. Obata, K. Abiko, and H. Kimura, Role of carbon in preventing the intergranular fracture in iron-phosphorus alloys, *Trans. Iron Steel Inst. Jpn.* **25**, 62 (1985).
- [11] S. Suzuki, S. Tanii, K. Abiko, and H. Kimura, Site competition between sulfur and carbon at grain boundaries and their effects on the grain boundary cohesion in iron, *Metall. Trans. A* **18**, 1109 (1991).
- [12] R. Wu, A. J. Freeman, and G. Olson, Effects of carbon on Fe-grain-boundary cohesion: First-principles determination, *Phys. Rev. B* **53**, 7504 (1996).
- [13] A. Ishii, J. Li, and S. Ogata, "Conjugate channeling" effect in dislocation core diffusion: Carbon transport in dislocated bcc iron, *PLoS ONE* **8**, e60586 (2013).
- [14] J. Wang, R. Janisch, G. K. Madsen, and R. Drautz, First-principles study of carbon segregation in bcc iron symmetrical tilt grain boundaries, *Acta Mater.* **115**, 259 (2016).
- [15] J. Cho, J. M. Rickman, H. M. Chan, and M. P. Harmer, Modeling of grain-boundary segregation behavior in aluminum oxide, *J. Am. Ceram. Soc.* **83**, 344 (2000).
- [16] Z. Li, A. M. Freborg, B. D. Hansen, and T. S. Srivatsan, Modeling the effect of carburization and quenching on the development of residual stresses and bending fatigue resistance of steel gears, *J. Mater. Eng. Perform.* **22**, 664 (2013).
- [17] Y.-G. Yang, Z.-L. Mi, M. Xu, Q. Xiu, J. Li, and H.-T. Jiang, Impact of intercritical annealing temperature and strain state on mechanical stability of retained austenite in medium Mn steel, *Mater. Sci. Eng. A* **725**, 389 (2018).
- [18] J. Zhang, W. Li, H. Wang, Q. Song, L. Lu, W. Wang, and Z. Liu, A comparison of the effects of traditional shot peening and micro-shot peening on the scuffing resistance of carburized and quenched gear steel, *Wear* **368**, 253 (2016).
- [19] S. Roy, G. T. C. Ooi, and S. Sundararajan, Effect of retained austenite on micropitting behavior of carburized AISI 8620 steel under boundary lubrication, *Materialia* **3**, 192 (2018).
- [20] B. Liu, W. Li, X. Lu, X. Jia, and X. Jin, The effect of retained austenite stability on impact-abrasion wear resistance in carbide-free bainitic steels, *Wear* **428**, 127 (2019).
- [21] S. Masoudi, G. Amirian, E. Saeedi, and M. Ahmadi, The effect of quench-induced residual stresses on the distortion of machined thin-walled parts, *J. Mater. Eng. Perform.* **24**, 3933 (2015).
- [22] R. Candela, S. Gelin, N. Mousseau, R. Veiga, C. Domain, M. Perez, and C. S. Becquart, Investigating the kinetics of the formation of a C Cottrell atmosphere around a screw dislocation in bcc iron: A mixed-lattice atomistic kinetic Monte-Carlo analysis, *J. Phys.: Condens. Matter* **33**, 065704 (2020).
- [23] F. El-Mellouhi, N. Mousseau, and L. J. Lewis, Kinetic activation-relaxation technique: An off-lattice self-learning kinetic Monte Carlo algorithm, *Phys. Rev. B* **78**, 153202 (2008).
- [24] N. Mousseau, L. K. Béland, P. Brommer, F. El-Mellouhi, J. F. Joly, G. K. N'tsouaglo, O. A. Restrepo, and M. Trochet, Following atomistic kinetics on experimental timescales with the kinetic Activation Relaxation Technique, *Comput. Mater. Sci.* **100**, 111 (2015).
- [25] L. K. Béland, P. Brommer, F. El-Mellouhi, J.-F. Joly, and N. Mousseau, Kinetic activation-relaxation technique, *Phys. Rev. E* **84**, 046704 (2011).
- [26] B. D. McKay, Practical graph isomorphism, *Congr. Numer.* **30**, 4587 (1981).
- [27] G. Barkema and N. Mousseau, Event-Based Relaxation of Continuous Disordered Systems, *Phys. Rev. Lett.* **77**, 4358 (1996).
- [28] R. Malek and N. Mousseau, Dynamics of Lennard-Jones clusters: A characterization of the activation-relaxation technique, *Phys. Rev. E* **62**, 7723 (2000).

- [29] E. Machado-Charry, L. K. Béland, D. Caliste, L. Genovese, T. Deutsch, N. Mousseau, and P. Pochet, Optimized energy landscape exploration using the *ab initio* based activation-relaxation technique, *J. Chem. Phys.* **135**, 034102 (2011).
- [30] A. F. Voter, Introduction to the kinetic Monte Carlo method, in *Radiation Effects in Solids*, edited by K. E. Sickafus, E. A. Kotomin, and B. P. Uberuaga, (Springer, Dordrecht, 2007), pp. 1–23.
- [31] H. Eyring, The activated complex and the absolute rate of chemical reactions, *Chem. Rev.* **17**, 65 (1935).
- [32] M. G. Evans and M. Polanyi, Some applications of the transition state method to the calculation of reaction velocities, especially in solution, *Trans. Faraday Soc.* **31**, 875 (1935).
- [33] K. J. Laidler and M. C. King, Development of transition-state theory, *J. Phys. Chem.* **87**, 2657 (1983).
- [34] J.-F. Joly, L. K. Béland, P. Brommer, F. El-Mellouhi, and N. Mousseau, Optimization of the kinetic activation-relaxation technique, an off-lattice and self-learning kinetic monte-carlo method, *J. Phys.: Conf. Ser.* **341**, 012007 (2012).
- [35] S. Mahmoud and N. Mousseau, Long-time point defect diffusion in ordered nickel-based binary alloys: How small kinetic differences can lead to completely long-time structural evolution, *Materialia* **4**, 575 (2018).
- [36] B. Puchala, M. L. Falk, and K. Garikipati, An energy basin finding algorithm for kinetic Monte Carlo acceleration, *J. Chem. Phys.* **132**, 134104 (2010).
- [37] M. Mendeleev, S. Han, D. Srolovitz, G. Ackland, D. Sun, and M. Asta, Development of new interatomic potentials appropriate for crystalline and liquid iron, *Philos. Mag.* **83**, 3977 (2003).
- [38] C. Becquart, J.-M. Raulot, G. Bencteux, C. Domain, M. Perez, S. Garruchet, and H. Nguyen, Atomistic modeling of an Fe system with a small concentration of C, *Comput. Mater. Sci.* **40**, 119 (2007).
- [39] R. G. Veiga, C. Becquart, and M. Perez, Comments on ‘Atomistic modeling of an Fe system with a small concentration of C’, *Comput. Mater. Sci.* **82**, 118 (2014).
- [40] R. G. Veiga, M. Perez, C. Becquart, C. Domain, and S. Garruchet, Effect of the stress field of an edge dislocation on carbon diffusion in α -iron: Coupling molecular statics and atomistic kinetic Monte Carlo, *Phys. Rev. B* **82**, 054103 (2010).
- [41] D. S. Tchitchekova, J. Morthomas, F. Ribeiro, R. Ducher, and M. Perez, A novel method for calculating the energy barriers for carbon diffusion in ferrite under heterogeneous stress, *J. Chem. Phys.* **141**, 034118 (2014).
- [42] E. Clouet, S. Garruchet, H. Nguyen, M. Perez, and C. S. Becquart, Dislocation interaction with c in α -Fe: A comparison between atomic simulations and elasticity theory, *Acta Mater.* **56**, 3450 (2008).
- [43] S. Plimpton, Fast parallel algorithms for short-range molecular dynamics, *J. Comput. Phys.* **117**, 1 (1995).
- [44] LAMMPS web site, <http://lammps.sandia.gov>.
- [45] See Supplemental Material at <http://link.aps.org/supplemental/10.1103/PhysRevMaterials.5.043605> for additional figures and tables.
- [46] W. Łojkowski, U. Södervall, S. Mayer, and W. Gust, The effect of pressure on indium diffusion along $\langle 001 \rangle$ tilt grain boundaries in copper bicrystals, *Interface Sci.* **6**, 187 (1998).
- [47] W. Łojkowski, Evidence for pressure effect on impurity segregation in grain boundaries and interstitial grain boundary diffusion mechanism, in *Defect and Diffusion Forum* (Trans Tech Publications, Pfaffikon, Switzerland, 1996), Vol. 129, p. 269–278.
- [48] P. Klugkist, A. Aleshin, W. Łojkowski, L. Shvindlerman, W. Gust, and E. Mittemeijer, Diffusion of Zn along tilt grain boundaries in Al: pressure and orientation dependence, *Acta Mater.* **49**, 2941 (2001).
- [49] B. B. Karki, D. B. Ghosh, and A. K. Verma, First-principles prediction of pressure-enhanced defect segregation and migration at MgO grain boundaries, *Am. Mineral.* **100**, 1053 (2015).
- [50] <http://normandmousseau.com>.